

First visual orbit for the prototypical colliding-wind binary WR 140

J. D. Monnier¹, Ming Zhao¹, E. Pedretti^{1,9}, R. Millan-Gabet², J.-P. Berger³, W. Traub⁴,
F.P.Schloerb⁵, T. ten Brummelaar⁶, H. McAlister⁶, S. Ridgway⁷, L. Sturmann⁶, J.
Sturmann⁶, N. Turner⁶, F. Baron¹, S. Kraus¹, A. Tannirkulam^{1,10}, P. M. Williams⁸

JDM: monnier@umich.edu

ABSTRACT

Wolf-Rayet stars represent one of the final stages of massive stellar evolution. Relatively little is known about this short-lived phase and we currently lack reliable mass, distance, and binarity determinations for a representative sample. Here we report the first visual orbit for WR 140(=HD193793), a WC7+O5 binary system known for its periodic dust production episodes triggered by intense colliding winds near periastron passage. The IOTA and CHARA interferometers resolved the pair of stars in each year from 2003–2009, covering most of the highly-eccentric, 7.9 year orbit. Combining our results with the recent improved double-line spectroscopic orbit of Fahed et al. (2011), we find the WR 140 system is located at a distance of 1.67 ± 0.03 kpc, composed of a WR star with $M_{\text{WR}} = 14.9 \pm 0.5 M_{\odot}$ and an O star with $M_{\text{O}} = 35.9 \pm 1.3 M_{\odot}$. Our precision

¹monnier@umich.edu: University of Michigan Astronomy Department, 941 Dennison Bldg, Ann Arbor, MI 48109-1090, USA.

²California Institute of Technology, NASA Exoplanet Science Institute, Pasadena, CA 91125, USA

³IPAG,CNRs/UMR 5571, Universite J. Fourier, BP-53, F-38041 Grenoble Cedex, France

⁴Jet Propulsion Laboratory, California Institute of Technology, M/S 301-355, 4800 Oak Grove Drive, Pasadena, CA 91109, USA

⁵University of Massachusetts, Department of Astronomy, Amherst, MA 01003-4610, USA

⁶The CHARA Array of Georgia State University, Mt. Wilson, CA, 91023, USA

⁷National Optical Astronomy Observatory, 950 N. Cherry Ave, Tucson AZ 85719. USA

⁸Institute for Astronomy, University of Edinburgh, Royal Observatory, Blackford Hill, Edinburgh, UK

⁹European Organisation for Astronomical Research in the Southern Hemisphere, Karl Schwarzschild Strasse 2, 85748 Garching bei Munchen

¹⁰Center for Micro Finance, The Institute for Financial Management and Research

orbit yields key parameters with uncertainties $\sim \times 6$ smaller than previous work and paves the way for detailed modeling of the system. Our newly measured flux ratios at the near-infrared H and Ks bands allow an SED decomposition and analysis of the component evolutionary states.

Subject headings: stars: binaries:visual, stars: individual (WR 140, HD 193793), stars: Wolf-Rayet, techniques: interferometric, infrared: stars

1. Introduction

Wolf-Rayet (WR) stars are evolved massive stars characterized by intense mass-loss through radiation-driven winds. These hot, emission-line stars are especially helium-rich, having lost most of their hydrogen envelope through winds or interaction with a companion. The range of progenitors that become WR stars is not well understood and establishing a massive star evolution sequence represents one of the most serious challenges for modern stellar theory (see recent review by Crowther 2007).

Concrete mass and distance determinations are crucial to making further progress, but this is difficult due to the large distances from Earth at which most WR stars lie. According to van der Hucht (2001), there are only 19 WR stars with mass estimates based on spectroscopic orbits and the vast majority of these are for short-period systems with periods between 1–100 days. Longer period binaries are less likely to have had interactions between the components but are difficult to characterize due to the lower orbital speeds.

The subject of this Letter is WR 140 (=HD 193793), a WR binary system with a 7.9 year period. Williams et al. (1987) first noticed mysterious episodic infrared variability and follow-up observations (Williams et al. 1990; Moffat et al. 1987) established the cause to be dust creation near periastron of a highly eccentric orbit, likely catalyzed in the colliding-wind interface between the WR star and O-star winds (Usov 1991). Since this time, WR 140 (WC7+O5) has been subject to many monitoring campaigns, including infrared (Williams et al. 2009), radio (White & Becker 1995), and in radial velocity (Fahed et al. 2011). Recently, progress towards a proper visual orbit was made by the single-epoch detection of the binary using the IOTA interferometer (Monnier et al. 2004) and through repeated imaging of the rotating colliding-wind region using the VLBA (Dougherty et al. 2005). Despite the wealth of data, mass estimates have suffered from large errors ($\sim 20\%$) due to lack of a high-quality visual orbit to go along with precise spectroscopic data.

In this paper, we report seven epochs of binary observations at the near-infrared H and Ks bands with the IOTA and CHARA interferometers. Our data span seven years allowing

us to construct the first complete visual orbit for WR 140. We combine this with recent spectroscopic work to determine precise masses and orbital parallax.

2. Observations

2.1. IOTA

Observations of WR 140 in 2003, 2004, and 2005 were obtained with the IOTA (Infrared-Optical Telescope Array) interferometer (Traub et al. 2003). IOTA was located on Mt. Hopkins (Arizona) and consisted of three 0.45-m telescopes that were movable among 17 stations along 2 orthogonal linear arms (telescopes A & C could move along the 35-m northeastern arm, while telescope B could move along the 15-m southeastern arm). By observing a target in many different array configurations, IOTA could synthesize an aperture $35\text{m} \times 15\text{m}$ (corresponding to an angular resolution of $\frac{\lambda}{B} \sim 5 \times 12$ milliarcseconds at $1.65\mu\text{m}$). The observations of WR 140 from 2003 were first reported in Monnier et al. (2004).

All of the IOTA observations included three simultaneous baselines using the broad band H filter and the light beams from the three telescopes were interfered using the single-mode IONIC3 combiner (Berger et al. 2003). Basic data reduction procedures were the same as described in several previous IOTA papers (e.g., Monnier et al. 2006) and final error estimation followed the study of the λ Vir binary by Zhao et al. (2007); we applied 2% relative and a $\Delta\mathcal{V}^2 = 0.02$ additive systematic errors to all our measured visibility amplitude \mathcal{V}^2 data. We found our closure phases were partially corrupted by bandwidth smearing effects and we only used \mathcal{V}^2 data for our orbit fitting (see detailed description and simulation of these effects explored by Zhao et al. 2007). Table 1 contains a detailed log of the IOTA observations.

2.2. CHARA

Observations of WR 140 in the years 2006, 2007, 2008, and 2009 were obtained with the Center for High Angular Resolution Astronomy (CHARA) Array. CHARA is located on Mt. Wilson (California) and consists of six fixed 1-m aperture telescopes with baselines ranging from 30 to 330m. CHARA is currently the longest baseline optical interferometer in the world and can reach angular resolutions of ~ 0.5 milli-arcseconds (mas) in the near-infrared. The CHARA facility and the two-beam CLASSIC combiner used in this work are described by ten Brummelaar et al. (2005).

Most of the CHARA observations were carried out in the Ks band although a few data points were taken in the H band. The observing dates, wavelengths, and baselines can be found in Table 1. We reduced the data using an IDL-based suite of routines written by one of us (JDM) and these have been previously described in Tannirkulam et al. (2008). For this paper, we adopted a 10% relative and a $\Delta\mathcal{V}^2 = 0.02$ additive error to account for systematic calibration errors*.

We have reported all the calibrators and adopted sizes in Table 1. Uniform Disk (UD) diameters of interferometer calibrators were generally estimated using *getCal*, an SED-fitting routine maintained and distributed by the NASA Exoplanet Science Institute (<http://nexsci.caltech.edu>), or SearchCal (Bonneau et al. 2006), a surface brightness algorithm maintained and distributed by the J. M. Mariotti Center (JMMC, <http://jmmc.fr>). We note that *getCal* does not produce as accurate diameter estimates as *searchCal* in general, but *getCal* can be employed on a wider variety of calibrator spectral types and was more useful in this current paper.

The final IOTA and CHARA calibrated \mathcal{V}^2 data were saved in OI-FITS format (Pauls et al. 2005) and all files are available upon request.

3. Analysis

We have interpreted our \mathcal{V}^2 data using a binary model. Here we describe the components of the model and our fitting results.

3.1. Description of binary model

Our model for WR 140 consists of two stars, each modelled as a uniform disk. The size of the O-star can be estimated based on the effective temperature and infrared flux estimate, while the WR-star size is affected by the optically-thick wind (we followed similar procedure as Millour et al. 2007, to account for wind opacity). We found that both stars are much smaller than the resolution of CHARA and so our final results are not sensitive to our adopted UD size of 0.05 mas for the WR star and 0.07 mas for the O-star.

The WR/O-star flux ratios at H band and Ks band were separately fitted but held

*The calibration errors were lower for IOTA-IONIC3 because of the use of single-mode fibers while CHARA-CLASSIC is a “free-space combiner” with only limited spatial filtering.

constant across all epochs. The near-infrared flux monitoring by Taranova & Shenavrin (2011) showed that 52% of the K-band emission during the 2009 epoch was from the outburst dust shell and was assumed to be over-resolved by CHARA. No other epochs were affected by dust emission. For a given set of orbital elements ($a, e, i, \omega, \Omega, P, T_0$), we can predict the separation and position angle at the time of each observation. The apparent brightness ratio can be affected by the finite bandwidth of the observations (“bandwidth-smearing”) and we have accounted for the square bandpasses of the H and Ks filter using the basic procedure described in Zhao et al. (2007). The bandwidth-smearing correction was insignificant for the short baseline IOTA data, but did affect the longer baseline CHARA data at the 5–10% level.

For visualization purposes, we also collected each year’s data and fitted for relative positions. The best fitting locations of the O-star relative to the WR star for each observation year has been included in Figure 1 and allows comparison with our final orbit fitting results. The size and shape of each epoch’s allowed region (an error ellipse containing the 68% confidence region) vary significantly from year to year due to differences in the quantity and quality of the \mathcal{V}^2 data. We also included the parameters of these best-fit locations in Table 2.

To validate our choice of this simple binary model, we also carried out model-independent image reconstructions for the 2003–2005 IOTA/IONIC3 data. We confirmed that the system is dominated by two point sources. We were interested to see if there could be any sign of the colliding wind zone between the stars, but no extra emission was seen in this region (at the level of a few percent of the peak emission). The brightest emission not coming from the two stars showed up to the North-East of the system in some epochs at the 2–5% level – likely an artifact from residual miscalibration.

3.2. Orbit fitting procedure

To arrive at our final orbital solutions, we fit directly to the \mathcal{V}^2 values. We carried out two different fitting exercises that differed in how we incorporated spectroscopic data.

First we wanted to carry out an orbital fit as independent as possible from the recent spectroscopic orbit of Fahed et al. (2011). This allows us to independently confirm the crucial orbital elements e and ω , although we adopted their values for the period (P) and time of periastron (T_0) in this procedure. The best-fitting orbital elements (reduced $\chi^2 = 0.52$) are compiled in the right column of Table 3. Error bars were estimated using 1000 bootstrap resamplings (Efron & Tibshirani 1993) of the data (grouped by night). This is the same procedure recently applied for the visual orbit of α Oph (Hinkley et al. 2011). In order

to capture the uncertainties in the Fahed et al. (2011) estimates for P and T_0 , we did not strictly fix these quantities during the bootstrap fits but rather used Monte Carlo sampling based on the Fahed et al. (2011) uncertainty estimates.

The IOTA+CHARA visual orbit compares favorably with the spectroscopically-determined orbital elements from Fahed et al. (2011):

- e : 0.8962 ± 0.0014 (Fahed’s orbit “This paper+M03”) compared to eccentricity $0.901^{+0.006}_{-0.004}$ (this work alone). These values are compatible and confirm the high orbit eccentricity.
- ω : $44.6^\circ \pm 1.1^\circ$ (Fahed’s orbit “This orbit+M03”) compared to $48.2^\circ \pm 1.3^\circ$ (this work alone). This is slightly discrepant, although note that one of the orbital solutions presented in the Fahed et al. (2011) report $\omega = 47.5^\circ$ (Fahed’s orbit “This paper”; middle solution in Table 2).

Much tighter constraints on the orbital elements can be attained by using the spectroscopic values from Fahed et al. (2011) as a *prior* in the visual orbit fit (the orbit labeled “This paper+M03”). The most important effect of this is to constrain the eccentricity, which is better determined by the Fahed et al. (2011) dataset that sampled the periastron period very densely. Our visual observations missed the fast-changing orbital motion in early 2009 and thus can not be expected to optimally constrain eccentricity.

The first column of Table 3 contains our best-fitting solution from the joint analysis (reduced $\chi^2 = 0.51$). We used the same bootstrap procedure to determine the error bars on each parameter. To visualize the range of orbits allowed by our solutions, we plotted all 1000 bootstrap orbits in Figure 1. As expected, the joint solution is better constraining, especially near periastron.

The last step in our analysis was to take the new orbital elements and use the spectroscopic K values from Fahed et al. (2011) to calculate masses and orbital parallax. Strictly speaking, since the K values depend slightly on the orbital elements themselves, we re-fitted the γ and K values for our orbital solutions using the radial velocity data in Fahed et al. (2011). This refinement is slightly more accurate than simply adopting the spectroscopic $a \sin i$ along with astrometry to derive inclination and distance. The final results for masses and distance are also included in Table 3.

Another way to view the remarkable quality of the fit is presented in Figure 2. Here we show the observed \mathcal{V}^2 as a function of the projected separation of the two components (joint orbital solution). This figure also shows the effect of bandwidth smearing for large projected separations.

4. Discussion and Future Work

The WR and O-star masses found here are similar to previous estimates (e.g. van der Hucht 2001) but with about $6\times$ smaller error bars ($\sim 3\text{--}4\%$). As has been seen in other WC binary systems, we find the WR star mass is less than $20 M_{\odot}$ and less than half the current mass of the O-star companion. These two qualities fit the interesting trend seen in the (six) WC stars with mass estimates (Crowther 2007). Our accurate distance will help to place these two stars in the Hertzsprung-Russel diagram for a stringent test of stellar evolution models that include mass-loss. This is only the second galactic WR star to have a distance measured through (orbital) parallax (the other is γ Vel; Millour et al. 2007). Note that the periastron distance of the orbit is 1.53 AU, which means the O-star companion is too distant to have affected the stellar evolution of the Wolf-Rayet star – unless the WR star progenitor experienced a red supergiant stage (see case of WR 104; Tuthill et al. 2008) or the orbit has drastically changed due to mass-loss.

The interferometry data allow us to measure the flux ratios of the two stars ($\frac{\text{Flux}_{\text{(WR)}}}{\text{Flux}_{\text{(O)}}}$) in the H- and Ks-bands for the first time. Our H-band IOTA data employed closure phases, allowing us to identify the Northwest component to be brightest in 2003. We have had to assume that this component is also brighter at K band since we lack closure phase data to break the 180° degeneracy of single-baseline data.

Based on our flux ratios, the IR-bright component has a significantly redder color than the IR-faint component, consistent with the IR-bright component being the WR star. The shape of the non-thermal radio emission (Dougherty et al. 2005) also identifies the Northwest (IR-bright) component in 2003 to be the WR star that is expected to possess the the higher-momentum wind.

Armed with this knowledge, we can decompose the combined spectral energy distribution (SED) into their component SEDs. For the combined system, we adopt (non-dusty) BVJHK magnitudes = (7.28, 6.89, 5.71, 5.35, 5.02) (Reed 2003; Taranova & Shenavrin 2011) and assume the O5III star has colors given by Martins & Plez (2006). The last ingredient we need is the least certain: the interstellar reddening. We will adopt the reddening law of Mathis (1990) with $R_V=3.1$ and with A_V spanning $A_V = 2.95$ from Morris et al. (1993) using the 2175\AA feature and $A_V = 2.06$ from SED colors (Conti & Vacca 1990)[†] – as you will see, the large uncertainty in A_V leads to large errors in our system luminosity despite our new well-constrained distance. We can now fix the H band ratio to 1.37 from our IOTA data and solve for the remaining flux ratios (modulo the A_V uncertainty). For $A_V = 2.95$, the flux

[†]Here, we have used the relation that $A_v = 1.1 A_V$ (e.g., Smith 1968)

ratios at BVJHK become (2.46, 1.64, 1.05, 1.37, 1.93); for $A_V = 2.06$ the flux ratios become (0.37, 0.35, 0.88, 1.37, 2.09). The observed flux ratio at Ks band (1.94 ± 0.06) is within the range seen here and is in good agreement with the high A_V case. Depending on which lines are used and which templates are adopted, Fahed et al. (2011) argue that the O-star might range from ~ 0.5 to $\sim 3\times$ brighter than the WR star in the optical band continuum – a wide range compatible with our derived flux ratios. Our prediction for V band flux ratio varies by a factor of 5 (!) because of A_V uncertainties and thus an interferometric measurement here could be exploited to strongly constrain the true reddening, a crucial component to luminosity determination which we now explore.

Using our new distance ($d = 1.67$ kpc) and the range of flux ratios, we find M_V for the O-star ranges from -6.11 and -5.94 and the M_V for the WR star ranges from -6.6 and -4.8. This would classify the O5 star as intermediate between giant and supergiant (cf. Martins & Plez 2006). The WR star luminosity class is hardly constrained but the high A_V case yields unrealistically high luminosities as judged by other WC7 stars with known distances (via cluster membership; van der Hucht 2001). In an attempt to reconcile the differences, we scaled the fluxes for a 70kK CMFGEN model for the WC7 star from Smith et al. (2002) to match the measured flux ratio of 1.37 in the H Band using a model SED for the O5 star from Martins et al. (2005). The WR/O5 flux ratios in V and v were found to be 1.05 and 0.73 respectively, that in V being affected by strong emission lines. The absolute magnitudes derived for the O5 star, $M_V = -6.37$ and -5.65 for high and low reddening extremes, are near or above those for supergiants, whereas those for the WC star, $M_v = -6.7$ and -5.9 are both anomalously high. Resolution of the uncertain interstellar reddening of WR 140 is beyond the scope of the present paper but is urgently required to exploit the determination of its parallax.

We expect our success here will motivate future observations of galactic Wolf-Rayet stars using today’s interferometers from visible to NIR wavelengths. The multi-wavelength flux ratios can help yield crucially-needed new estimates of interstellar reddening and the possibility to combine spectroscopic orbits with new interferometric visual orbits will allow accurate distance, mass, and luminosity measurements for a substantially larger set of galactic WR stars. Such a dataset is important to test the current massive stellar evolution paradigm that tells us how main-sequence O-stars move through the various stages of Red Supergiant, Wolf-Rayet (WN & WC) and Luminous Blue Variable before ultimately becoming a Supernova.

We have appreciated discussions with Tony Moffat, Peter Tuthill, Debra Wallace, Bill Danchi, Sean Dougherty, and Remi Fahed during the (long) course of this work. We thank SAO, U. Mass, NSF AST-0138303, NSF AST-0352723, and NASA NNG05G1180G for sup-

porting IOTA development and operations. We also acknowledge funding from GSU, the Keck Foundation, and NSF AST-0908253 for the CHARA Array. IONIC-3 was developed by LAOG (now IPAG) and LETI in the context of the IONIC collaboration (LAOG, IMEP, LETI), funded by the CNRS and CNES (France). Lastly we thank NSF AST-0807577 for support of University of Michigan researchers in this work. EP received funding from a Michelson Postdoctoral Fellowship and a Scottish Universities Physics Alliance (SUPA) advanced fellowship. PMW is grateful to the Institute for Astronomy for hospitality and continued access to the facilities of the Royal Observatory, Edinburgh. This research has made use of the SIMBAD database, operated at CDS, Strasbourg, France, and NASA’s Astrophysics Data System (ADS) Bibliographic Services.

Facility: IOTA (IONIC3), CHARA (CLASSIC)

REFERENCES

- Berger, J., Haguenaue, P., Kern, P. Y., Rousselet-Perraut, K., Malbet, F., Gluck, S., Lagny, L., Schanen-Duport, I., Laurent, E., Delboulbe, A., Tatulli, E., Traub, W. A., Carleton, N., Millan-Gabet, R., Monnier, J. D., & Pedretti, E. 2003, in *Interferometry for Optical Astronomy II*. Edited by Wesley A. Traub . Proceedings of the SPIE, Volume 4838, pp. 1099-1106 (2003)., 1099–1106
- Bonneau, D., Clausse, J.-M., Delfosse, X., Mourard, D., Cetre, S., Chelli, A., Cruzalèbes, P., Duvert, G., & Zins, G. 2006, *A&A*, 456, 789
- Conti, P. S. & Vacca, W. D. 1990, *AJ*, 100, 431
- Crowther, P. A. 2007, *ARA&A*, 45, 177
- Dougherty, S. M., Beasley, A. J., Claussen, M. J., Zauderer, B. A., & Bolingbroke, N. J. 2005, *ApJ*, 623, 447
- Efron, B. & Tibshirani, R. J. 1993, *An introduction to the bootstrap* (New York: Chapman and Hall)
- Fahed, R., Moffat, A. F. J., Zorec, J., Eversberg, T., Chené, A.-N., Alves, F., Arnold, W., Bergmann, T., Carreira, L. F. G., Dias, F. M., Fernando, A., Gallego, J. S., Hunger, T., Knapen, J. H., Leadbeater, R., Morel, T., Rauw, G., Reinecke, N., Ribeiro, J., Romeo, N., dos Santos, E. M., Schanne, L., Stahl, O., Stober, B., Stober, B., Viegas, N. G. C., Vollmann, K., Corcoran, M. F., Dougherty, S. M., Pittard, J. M., Pollock, A. M. T., & Williams, P. M. 2011, *MNRAS*, in press

- Hinkley, S., Monnier, J. D., Oppenheimer, B. R., Roberts, Jr., L. C., Ireland, M., Zimmerman, N., Brenner, D., Parry, I. R., Martinache, F., Lai, O., Soummer, R., Sivaramakrishnan, A., Beichman, C., Hillenbrand, L., Zhao, M., Lloyd, J. P., Bernat, D., Vasisht, G., Crepp, J. R., Pueyo, L., Shao, M., Perrin, M. D., King, D. L., Bouchez, A., Roberts, J. E., Dekany, R., & Burruss, R. 2011, *ApJ*, 726, 104
- Martins, F. & Plez, B. 2006, *A&A*, 457, 637
- Martins, F., Schaerer, D., & Hillier, D. J. 2005, *A&A*, 436, 1049
- Mathis, J. S. 1990, *ARA&A*, 28, 37
- Millour, F., Petrov, R. G., Chesneau, O., Bonneau, D., Dessart, L., Bechet, C., Tallon-Bosc, I., Tallon, M., Thiébaud, E., Vakili, F., Malbet, F., Mourard, D., Antonelli, P., Beckmann, U., Bresson, Y., Chelli, A., Dugué, M., Duvert, G., Gennari, S., Glück, L., Kern, P., Lagarde, S., Le Coarer, E., Lisi, F., Perraut, K., Puget, P., Rantakyö, F., Robbe-Dubois, S., Roussel, A., Tatulli, E., Weigelt, G., Zins, G., Accardo, M., Acke, B., Agabi, K., Altariba, E., Arezki, B., Aristidi, E., Baffa, C., Behrend, J., Blöcker, T., Bonhomme, S., Busoni, S., Cassaing, F., Clausse, J.-M., Colin, J., Connot, C., Delboulbé, A., Domiciano de Souza, A., Driebe, T., Feautrier, P., Ferruzzi, D., Forveille, T., Fossat, E., Foy, R., Fraix-Burnet, D., Gallardo, A., Giani, E., Gil, C., Glentzlin, A., Heiden, M., Heininger, M., Hernandez Utrera, O., Hofmann, K.-H., Kamm, D., Kiekebusch, M., Kraus, S., Le Contel, D., Le Contel, J.-M., Lesourd, T., Lopez, B., Lopez, M., Magnard, Y., Marconi, A., Mars, G., Martinot-Lagarde, G., Mathias, P., Mège, P., Monin, J.-L., Mouillet, D., Nussbaum, E., Ohnaka, K., Pacheco, J., Perrier, C., Rabbia, Y., Rebattu, S., Reynaud, F., Richichi, A., Robini, A., Sacchettini, M., Schertl, D., Schöller, M., Solscheid, W., Spang, A., Stee, P., Stefanini, P., Tasso, D., Testi, L., von der Lühe, O., Valtier, J.-C., Vannier, M., & Ventura, N. 2007, *A&A*, 464, 107
- Moffat, A. F. J., Lamontagne, R., Williams, P. M., Horn, J., & Seggewiss, W. 1987, *ApJ*, 312, 807
- Monnier, J. D., Berger, J.-P., Millan-Gabet, R., Traub, W. A., Schloerb, F. P., Pedretti, E., Benisty, M., Carleton, N. P., Haguenauer, P., Kern, P., Labeye, P., Lacasse, M. G., Malbet, F., Perraut, K., Pearlman, M., & Zhao, M. 2006, *ApJ*, 647, 444
- Monnier, J. D., Traub, W. A., Schloerb, F. P., Millan-Gabet, R., Berger, J.-P., Pedretti, E., Carleton, N. P., Kraus, S., Lacasse, M. G., Brewer, M., Ragland, S., Ahearn, A., Coldwell, C., Haguenauer, P., Kern, P., Labeye, P., Lagny, L., Malbet, F., Malin, D.,

- Maymounkov, P., Morel, S., Papaliolios, C., Perraut, K., Pearlman, M., Porro, I. L., Schanen, I., Souccar, K., Torres, G., & Wallace, G. 2004, *ApJ*, 602, L57
- Morris, P. W., Brownsberger, K. R., Conti, P. S., Massey, P., & Vacca, W. D. 1993, *ApJ*, 412, 324
- Pauls, T. A., Young, J. S., Cotton, W. D., & Monnier, J. D. 2005, *PASP*, 117, 1255
- Reed, B. C. 2003, *AJ*, 125, 2531
- Smith, L. F. 1968, *MNRAS*, 140, 409
- Smith, L. J., Norris, R. P. F., & Crowther, P. A. 2002, *MNRAS*, 337, 1309
- Tannirkulam, A., Monnier, J. D., Harries, T. J., Millan-Gabet, R., Zhu, Z., Pedretti, E., Ireland, M., Tuthill, P., ten Brummelaar, T., McAlister, H., Farrington, C., Goldfinger, P. J., Sturmman, J., Sturmman, L., & Turner, N. 2008, *ApJ*, 689, 513
- Taranova, O. G. & Shenavrin, V. I. 2011, *Astronomy Letters*, 37, 30
- ten Brummelaar, T. A., McAlister, H. A., Ridgway, S. T., Bagnuolo, Jr., W. G., Turner, N. H., Sturmman, L., Sturmman, J., Berger, D. H., Ogden, C. E., Cadman, R., Hartkopf, W. I., Hopper, C. H., & Shure, M. A. 2005, *ApJ*, 628, 453
- Traub, W. A., Ahearn, A., Carleton, N. P., Berger, J., Brewer, M. K., Hofmann, K., Kern, P. Y., Lacasse, M. G., Malbet, F., Millan-Gabet, R., Monnier, J. D., Ohnaka, K., Pedretti, E., Ragland, S., Schloerb, F. P., Souccar, K., & Weigelt, G. 2003, in *Interferometry for Optical Astronomy II*. Edited by Wesley A. Traub. *Proceedings of the SPIE*, Volume 4838, pp. 45-52 (2003)., 45–52
- Tuthill, P. G., Monnier, J. D., Lawrance, N., Danchi, W. C., Owocki, S. P., & Gayley, K. G. 2008, *ApJ*, 675, 698
- Usov, V. V. 1991, *MNRAS*, 252, 49
- van der Hucht, K. A. 2001, *New A Rev.*, 45, 135
- White, R. L. & Becker, R. H. 1995, *ApJ*, 451, 352
- Williams, P. M., Marchenko, S. V., Marston, A. P., Moffat, A. F. J., Varricatt, W. P., Dougherty, S. M., Kidger, M. R., Morbidelli, L., & Tapia, M. 2009, *MNRAS*, 395, 1749

- Williams, P. M., van der Hucht, K. A., Florkowski, D. R., Pollock, A. M. T., & Wamsteker, W. M. 1987, in IAU Symposium, Vol. 122, Circumstellar Matter, ed. I. Appenzeller & C. Jordan, 453–454
- Williams, P. M., van der Hucht, K. A., Pollock, A. M. T., Florkowski, D. R., van der Woerd, H., & Wamsteker, W. M. 1990, MNRAS, 243, 662
- Zhao, M., Monnier, J. D., Torres, G., Boden, A. F., Claret, A., Millan-Gabet, R., Pedretti, E., Berger, J.-P., Traub, W. A., Schloerb, F. P., Carleton, N. P., Kern, P., Lacasse, M. G., Malbet, F., & Perraut, K. 2007, ApJ, 659, 626

Table 1. Observing log for WR140. All calibrated OI-FITS data available upon request.

Orbital Phase ^a	Date (UT)	Interferometer (Configuration)	λ_0 (μm)	Bandwidth (μm)
2.296	2003Jun17	IOTA ^b (A35C15C10)	1.650	0.248
2.406	2004Apr30	IOTA (A35B15C10)	1.650	0.248
2.407	2004May01	IOTA (A35B15C10)	1.650	0.248
2.417	2004May30	IOTA (A35B15C10)	1.650	0.248
2.417	2004Jun01	IOTA (A35B15C10)	1.650	0.248
2.418	2004Jun04	IOTA (A35B15C10)	1.650	0.248
2.419	2004Jun05	IOTA (A35B15C10)	1.650	0.248
2.419	2004Jun06	IOTA (A35B15C10)	1.650	0.248
2.547	2005Jun11	IOTA (A35B15C10)	1.650	0.248
2.547	2005Jun13	IOTA (A35B15C10)	1.650	0.248
2.548	2005Jun14	IOTA (A35B15C10)	1.650	0.248
2.548	2005Jun15	IOTA (A35B15C10)	1.650	0.248
2.548	2005Jun16	IOTA (A35B15C10)	1.650	0.248
2.549	2005Jun17	IOTA (A35B15C10)	1.650	0.248
2.549	2005Jun18	IOTA (A35B15C10)	1.650	0.248
2.698	2006Aug22	CHARA ^c (W2-E2)	2.133	0.350
2.799	2007Jun11	CHARA (W2-E2)	1.673	0.274
2.800	2007Jun13	CHARA (W2-E2)	2.133	0.350
2.926	2008Jun14	CHARA (W2-E2)	1.673	0.274
2.927	2008Jun16	CHARA (W2-S1)	2.133	0.350
2.927	2008Jun17	CHARA (W1-S2)	2.133	0.350
2.928	2008Jun18	CHARA (W1-S2)	2.133	0.350
3.054	2009Jun20	CHARA (W1-S2)	2.133	0.350
3.055	2009Jun22	CHARA (W1-S2)	2.133	0.350
3.055	2009Jun23	CHARA (S2-E2)	2.133	0.350
3.056	2009Jun25	CHARA (S2-E2)	2.133	0.350

^aOrbital phase assuming $T_0 = 2446156.2$ (MJD), $P = 2896.5$ days (Fahed et al. 2011).

^bIOTA calibration employed the following calibrators (all sizes were estimated using getCal): HD 192985 (0.46 ± 0.06 mas), HD 193631 (0.31 ± 0.28 mas), HD 126035 (0.78 ± 0.24 mas), HD 193664 (0.58 ± 0.05 mas), HD 193961 (0.24 ± 0.06 mas)

^cCHARA calibration employed the following calibrators (all sizes estimated using getCal, except HD196360): HD 192985 (0.46 ± 0.06 mas), HD 193631 (0.31 ± 0.28 mas), HD 196360 (0.61 ± 0.05 mas), HD 192640 (0.40 ± 0.15 mas), HD 195194 (0.63 ± 0.13 mas)

Table 2. Position of O-star with respect to WR star

Mean Date (UT)	Relative Position		Error Ellipse ^a		
	East (mas)	North (mas)	Major (mas)	Minor (mas)	PA Major (E of N)
2003Jun17	5.70	-11.31	0.87	0.30	-86
2004May25	6.87	-11.33	0.34	0.11	-61
2005Jun15	7.36	-10.16	0.37	0.11	-57
2006Aug22	6.97	-7.14	4.85	0.26	112
2007Jun12	5.73	-4.18	1.25	0.10	-28
2008Jun17	3.51	-0.76	0.11	0.05	51
2009Jun23	0.86	-5.46	0.70	0.13	-47

^aError ellipse contains 68% confidence interval and is specified by the \pm error in the two orthogonal directions (in milliarcseconds) specified by the position angle of the ellipse major axis (degrees East of North). See Figure 1 for graphical representation.

Table 3. Orbital parameters for WR140 (adopting WR as primary star, O as secondary star)

Parameter	This work with Fahed et al. (2011) prior	This work alone ^a
Flux Ratio ^b (H band)	1.37±0.03	
Flux Ratio (Ks band)	1.94±0.06	
Semi-Major Axis (mas)	8.82±0.05	8.99 ^{+0.16} _{-0.22}
Eccentricity	0.8964 ^{+0.0004} _{-0.0007}	0.901 ^{+0.006} _{-0.004}
Inclination (deg)	119.6±0.5	118.9 ^{+1.3} _{-0.5}
ω (deg)	46.8±0.4	48.2±1.9
Ω (deg)	353.6±0.4	354.2 ^{+0.9} _{-0.5}
Period (days)	2896.35±0.20	(2896.5 ^{+0.2} _{-1.5})
T_0 (MJD)	46154.8±0.8	(46155.7 ^{+2.6} _{-3.3})
$\sum \chi^2/\text{DOF}$	0.51	0.52
Derived Physical Quantities ^c		
Distance (kpc)	1.67±0.03	1.60 ^{+0.11} _{-0.07}
M_{WR} (M_{\odot})	14.9±0.5	13.9 ^{+1.9} _{-1.2}
M_{O} (M_{\odot})	35.9±1.3	33.1 ^{+4.5} _{-2.8}

^aAll orbital elements were fitted to the visual orbit date presented here, except for the P and T_0 , which were adopted from Fahed et al. (2011).

^bFlux ratio is $\frac{\text{WR flux density}}{\text{O5 flux density}}$.

^cThe visual orbit above and the spectroscopic data from Fahed et al. (2011) were combined to derive the orbital parallax and relative masses. We emphasize that the high precision on the mass and distance requires both the visual orbit presented here and high quality spectroscopic data of Fahed et al. (2011).

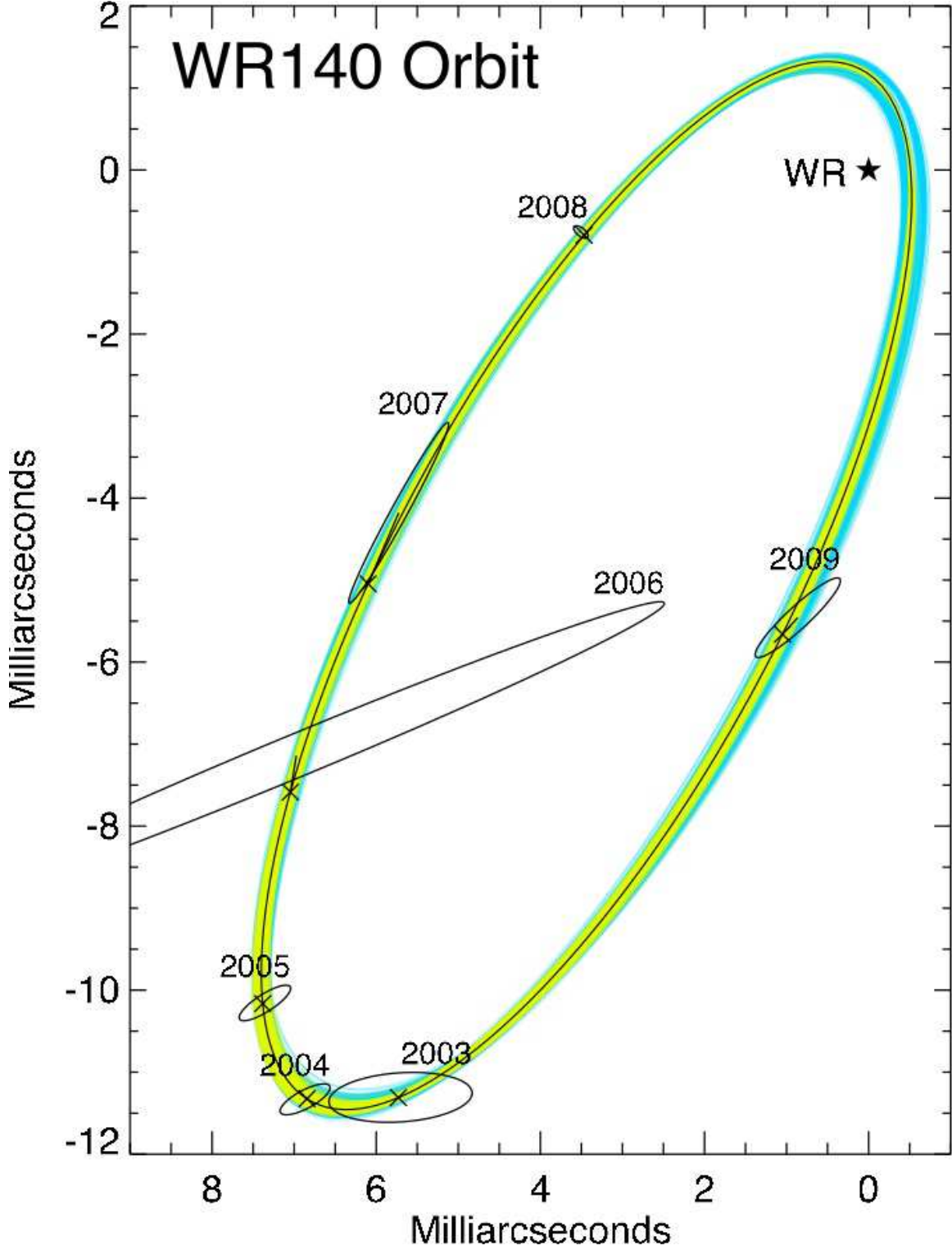


Fig. 1.— This figure shows the $3\text{-}\sigma$ band of allowed orbits based on our visual data alone (thick blue band) and for the more-constraining, joint visual/spectroscopic solution (yellow band). The best fit joint solution is shown with solid line. For each year, the data were analyzed separately and the positions of the O star with respect to WR star are shown here, marked by error ellipses (see Table 2). The best-fit orbit prediction for each epoch is connected to each corresponding error ellipse.

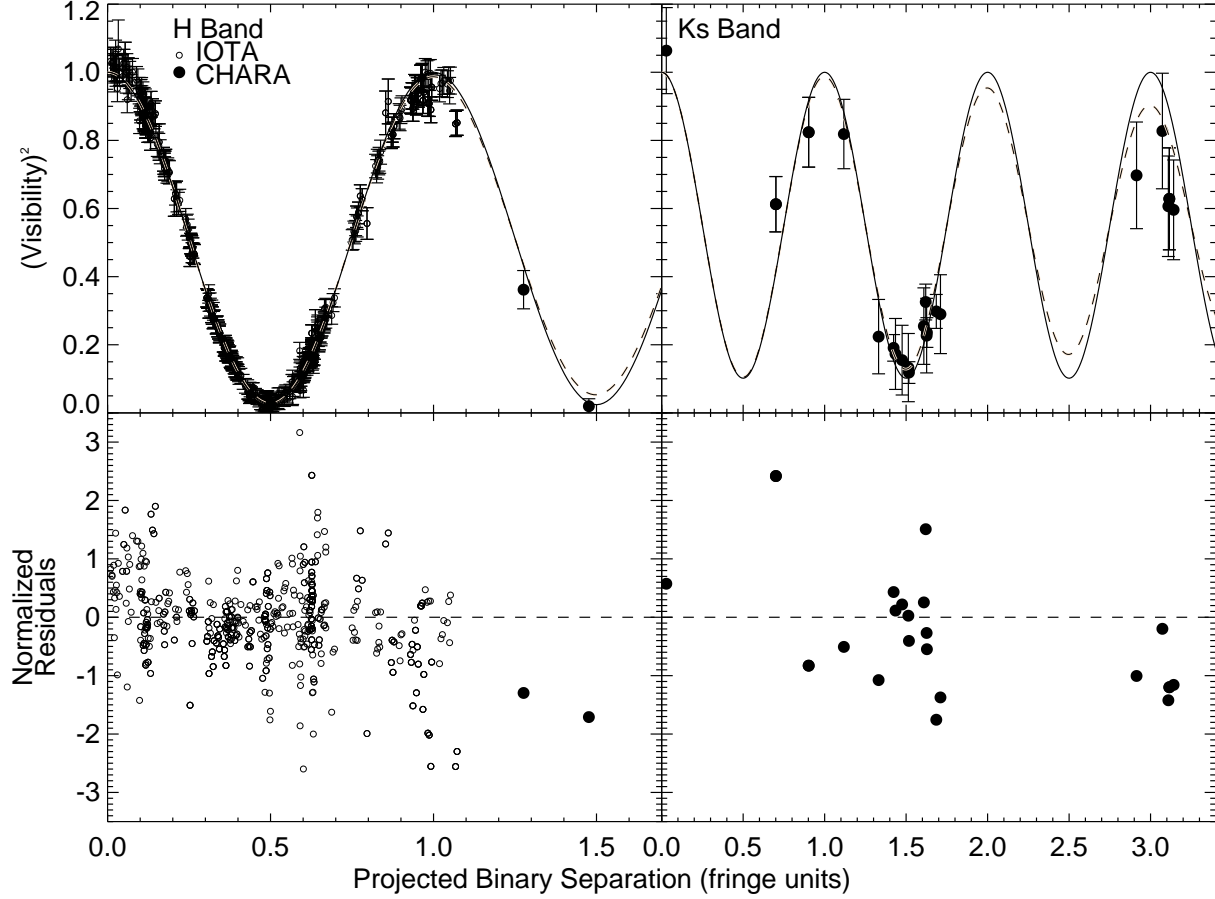


Fig. 2.— Here we plot the observed visibility data as a function of the projected binary separation of our best-fitting joint model. We have plotted the expected curve both for no bandwidth smearing (solid line) and for the appropriate level we used in this work (dashed line). The bottom panels show the residuals between data and model normalized by the data errors. Note the visibility for the CHARA 2009 data was boosted by factor of 2.1 to account for the extra over-resolved emission by the short-lived dust shell created at periastron (48% stellar emission, 52% dust; Taranova & Shenavrin 2011).